Applied Catalysis B: Environmental 233 (2018) 226–233

Contents lists available at ScienceDirect

Applied Catalysis B: Environmental

journal homepage: www.elsevier.com/locate/apcatb

Novel hydrothermal electrodeposition to fabricate mesoporous film of $Ni_{0.8}Fe_{0.2}$ nanosheets for high performance oxygen evolution reaction

Mengqi Yao[a], Ni Wang[a,b], Wencheng Hu[a,*], Sridhar Komarneni[b,*]

[a] Center of Applied Chemistry, University of Electronic Science & Technology of China, Chengdu, China
[b] Materials Research Institute and Department of Ecosystem Science and Management Materials Research Laboratory, The Pennsylvania State University, PA, USA

ARTICLE INFO

Keywords:
Mesoporous alloy films
$Ni_{0.8}Fe_{0.2}$ film
Hydrothermal electrodeposition
OER

ABSTRACT

Here, we report a new synthetic strategy to fabricate mesoporous film of $Ni_{0.8}Fe_{0.2}$ nanosheets for high performance oxygen evolution reaction (OER). Mesoporous $Ni_{0.8}Fe_{0.2}$ film self-supported on stainless steel mesh (SLS) was prepared via a novel hydrothermal electrodeposition process. Hydrothermally driven electrodeposition method showed significant advantages toward OER: (1) high temperature makes H_2 generated on the cathode to overflow faster. Both the gas generated on the cathode and hydrothermal condition impacted coating surface, hence, the film possessed more active sites to improve OER properties and (2) hydrothermal condition improved the crystallization of the coating leading to excellent electrode stability under OER test. The mesoporous $Ni_{0.8}Fe_{0.2}$ film exhibited an overpotential of 206 mV at 10 mA cm^{-2} (i.e., 1.436 V vs. RHE), a Tafel slope of 64 mV dec^{-1} and excellent stability after 2×10^5 s (more than 55 h) at 10 mA cm^{-2}. The superior OER properties could be attributed to the film's novel synthetic process, porous structure and high electrical conductivity. This work shows a new strategy to fabricate mesoporous alloy films as OER catalysts.

1. Introduction

With increasing concerns for environment and demand for energy, renewable and sustainable energy sources have attracted considerable interest as substituents for fossil fuels [1–3]. Among sustainable energy sources, hydrogen, with its high mass-specific energy density and environmental friendly characteristic, has been considered as a promising next generation energy source [4,5]. Electrochemical water splitting is an effective approach to generate hydrogen [6,7]. The oxygen evolution reaction (OER) is an anodic reaction of water splitting, which is a complex four proton and four electron transfer reaction ($4OH^- \rightarrow 2H_2O + 4e^- + O_2$ in alkaline conditions) [8,9]. The OER impedes the overall efficiency of water electrolysis as it is a kinetically sluggish process, which is the main challenge to overcome [10]. RuO_2 and IrO_2 have been identified as efficient OER catalysts because of their low overpotential and small Tafel slope [11,12]. However, their high cost and toxicity limit their large scale applications [13]. Therefore, exploring low cost and high catalytic activity catalysts based on earth-abundant metals, increasingly has been the focus of current research [14,15].

Over the past decades, nickel (Ni) and iron (Fe) based materials have been extensively investigated for OER catalysts because of the high OER performance and low cost of first-row transition metals [16–19]. Various NiFe based materials were designed for OER catalysts recently, including NiFe NPs [20], NiFe oxide [21], NiFe hydroxide [22], NiFe sulfide [23], NiFe selenide [24] and NiFe/C compound [25]. However, the above-mentioned NiFe based electrocatalysts have the following problems: low stability and poor conductivity which limit their catalytic properties. Coupling Ni and Fe based materials with conductive substrate is a valid approach to improve catalytic performance because appropriate substrates possess features such as good conductivity, abundant active sites and mechanical stability [26,27].

In addition, synthesis of porous nanomaterials with high surface area is widely acknowledged to be an attractive way to enhance catalytic performance [28,29]. High specific surface area was determined to be in favor of the diffusion of electrolyte and oxygen release [30]. Also, it can expose more active sites and defects for the electrocatalysis, which can control surface and electronic properties of OER catalysts, and bring in high catalytic activity [31,32]. Therefore, constructing nanomaterials with large specific surface area is a key challenge for OER catalysts. For instance, Liu et al. fabricated mesoporous $NiFe_2O_4$ nanorods as efficient oxygen evolution catalyst, which shows overpotential of 342 mV at 10 mA cm^{-2} and a Tafel slope of 44 mV dec^{-1} [33] while Zhang et al. synthesized NiFe LDH hollow microspheres with small onset overpotential of 239 mV at 10 mA cm^{-2} and a low Tafel slope of 53 mV dec^{-1} [34].

* Corresponding authors.
E-mail addresses: huwc@uestc.edu.cn (W. Hu), sxk7@psu.edu (S. Komarneni).

https://doi.org/10.1016/j.apcatb.2018.04.009
Received 18 December 2017; Received in revised form 31 March 2018; Accepted 5 April 2018
Available online 06 April 2018
0926-3373/

As reported in previous studies, most NiFe based OER catalysts are powders. They are coated onto the surface of conductive substrates with the help of binders [15,33,34]. The use of binders, however, reduce the conductivity of electrode giving rise to degraded OER performance. Another common phenomenon, which is a disadvantage is that the glued OER catalysts tend to peel off and aggregate during long-time electrochemical operations [35,36]. Electrodeposited metal alloy coatings onto the surface of substrates have also been wildly investigated as OER catalysts. However, the coatings usually show poor electrocatalytic performance because only the surface layers are in contact with electrolyte. Therefore, exploring a new strategy to electrodeposit metal alloys with abundant active sites for OER catalysts is of great interest.

Herein, we proposed and investigated hydrothermal electrodeposition method, for the first time, to fabricate mesoporous $Ni_{0.8}Fe_{0.2}$ film self-supported on SLS as an OER catalyst. Compared with traditional electrodeposition, hydrothermally driven electrodeposition possesses the following advantages: (1) higher temperature (110 °C) of hydrothermal electrodeposition method makes gas (H_2) generated on the cathode to overflow faster than that of traditional electrodeposition method (50–60 °C). Also, high temperature facilitates plating solution to gasify and lead to high pressure environment inside the confined space of Teflon autoclave. Both, the gas generated on the cathode and higher pressure impact the coating surface and hence, the film possesses more active sites to boost OER properties; (2) by calculating the size of NiFe particles, we found that the crystallization of the coating is better than that of traditional electrodeposition method so that the electrode presents excellent stability under OER test. The mesoporous $Ni_{0.8}Fe_{0.2}$ film synthesized here showed significantly enhanced electrochemical active area of 25.3 mF cm^{-2}, a low overpotential of 206 mV at 10 mA cm^{-2} and a small Tafel slope of 64 mV dec^{-1}. The newly developed process also led to an excellent stability for a long time of up to 2×10^5 s (more than 55 h) at 10 mA cm^{-2}, which is better than that achieved by traditional electrodeposition method. The mesoporous $Ni_{0.8}Fe_{0.2}$ film displayed a low overpotential, small Tafel slope and excellent stability due to its porous structure resulting from the novel synthesis process.

2. Experimental

2.1. Synthesis of electrocatalysts $Ni_{0.8}Fe_{0.2}$ film

The binary NiFe film was prepared via a novel hydrothermal electrodeposition method, which is reported for the first time to synthesize oxygen evolution reaction (OER) catalysts. Briefly, 12.6 g nickel sulfate hexahydrate and 6.6 g iron sulfate hexahydrate were dissolved in a mixture of 60 ml distilled water and 5 ml methanol followed by the addition of 2.4 g boric acid. Methanol was used to prevent ferrous iron from being oxidized and boric acid was used as a pH regulator. The solution was stirred for 30 min under N_2 condition. Then the transparent solution was transferred into a 100 ml Teflon autoclave. A piece of cleaned stainless steel mesh (304 L, 300 mesh) with a size of 2×3 cm^2 was used as cathode and 2×3 cm^2 nickel sheet with iron wire was used as anode. The autoclave was put inside the oven at 110 °C for n minutes (n = 10, 20, 30) with current density of 20 mA cm^{-2}. The binary NiFe metallic film was electrodeposited on the surface of stainless steel mesh. The NiFe film was washed with distilled water and ethanol for 6 times and dried at 100 °C under vacuum condition.

2.2. Synthesis of mesoporous $Ni_{0.8}Fe_{0.2}$ film

Mesoporous $Ni_{0.8}Fe_{0.2}$ film was fabricated via two steps. Firstly, 12.6 g nickel sulfate hexahydrate, 6.6 g iron sulfate hexahydrate, 7.3 g Zinc sulfate heptahydrate and 2.4 g boric acid were dissolved in a mixture of 60 ml distilled water and 5 ml methanol. Ternary NiFeZn film was synthesized by hydrothermal electrodeposition process, which is same as the synthesis of the above $Ni_{0.8}Fe_{0.2}$ film. The time of electrodeposition was 20 min. The NiFeZn film was washed with distilled water. Secondly, the NiFeZn film was immersed in 0.2 M KOH solution under N_2 condition for 7 days at room temperature. KOH solution was changed daily. Zn as template was reacted with KOH to construct mesoporous structure. Then the mesoporous $Ni_{0.8}Fe_{0.2}$ film was collected by washing with ethyl alcohol and dried at 100 °C in a vacuum. The resultant mass loading of mesoporous $Ni_{0.8}Fe_{0.2}$ film (~5.6 mg cm^{-2}) was roughly obtained by weighing the SLS before and after deposition of the final as-prepared sample.

2.3. Characterization of materials

The crystalline phases were characterized by X-ray diffraction (XRD) using an X-ray diffractometer (Smartlab9, Pigaku, Japan.). The micro morphologies were observed by field emission scanning electron microscope (FESEM) (Inspect F, FEI Co., U.S.) and high resolution transmission electron microscope (HRTEM) (Libra 200FE, Germany). N_2 adsorption/desorption isotherms were determined (JW-BK112 Surface Area Analyzer, Beijing JWGB, China) to analyze specific surface area and pore size diameter. The atomic composition was investigated by energy dispersive spectrometer (Inspect F, FEI Co., U.S.) and X-ray photoelectron spectroscopy (Thermo ESCALAB 250XI, Thermo Fisher Scientific, U.S.).

2.4. Electrochemical measurement

The electrochemical station (PGSTAT302N, Netherlands) was employed to test OER properties under a standard three-electrode system. 1 M KOH solution saturated by O_2 (99.999%) was used as electrolyte, 1×1 cm^2 NiFe film supported on SLS was used as working electrode. Pt/C wire and Hg/HgO electrode were used as counter electrode and reference electrode, respectively. Linear sweep voltammetry (LSV) was performed in 1.0 M KOH solution from 0 to 1.0 V at a scan rate of 5 mV s^{-1}. Electrochemical impedance spectroscopy (EIS) was measured at open circuit voltages from 10^6 to 10^{-2} Hz. Durability test was performed by chronopotentiometry at a constant current density of 10 mA cm^{-2}. All the potentials in this paper were versus the reversible hydrogen electrode (RHE) according to the following equation:

E(RHE) = E(Hg/HgO) + 0.059 pH + 0.098 V. The overpotential (η) corresponds to the equation η = E(RHE)-1.23 V.

3. Result and discussion

Mesoporous $Ni_{0.8}Fe_{0.2}$ film was prepared via two steps (see details in experimental section). Fig. 1 depicts the schematic of the synthesis process including the hydrothermally driven electrodeposition and etching of template. Stainless steel (SLS) mesh was chosen as a substrate due to its good conductivity and excellent stability, which are beneficial for OER performance. First, under the action of current, similar ionic electronegativity scales of Ni^{2+}, Fe^{2+} and Zn^{2+} [37] suggest their reduction to form ternary NiFeZn film of nanosheets on SLS at 110 °C in Teflon autoclave. Zinc grows on SLS in situ, which is used as a sacrificial template to construct porous structure. Second, NiFeZn film was etched by KOH and methanol mixed solution under high-purity N_2 condition to remove template (Zn). Finally, mesoporous NiFe film on SLS was obtained. This film structure evolution can enhance abundant catalytic sites and make mass transportation easy for oxygen evolution reaction (OER) [38]. In this paper, we will discuss six kinds of OER catalysts including mesoporous $Ni_{0.8}Fe_{0.2}$ film, $Ni_{0.8}Fe_{0.2}$-X film (x is time of electrodeposition, x = 10, 20 or 30 min), SLS and IrO_2/C. The IrO_2/C catalyst was prepared using the same procedure as has been recently reported [11] and used here as a control.

Morphological features and microstructure of mesoporous $Ni_{0.8}Fe_{0.2}$ film were analyzed by scanning electron microscope (SEM) and

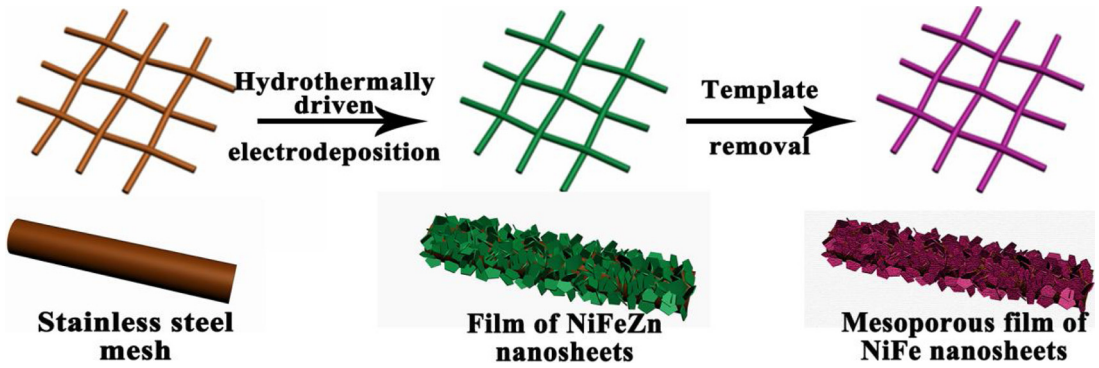

Fig. 1. A schematic of the synthesis of mesoporous $Ni_{0.8}Fe_{0.2}$ film on SLS.

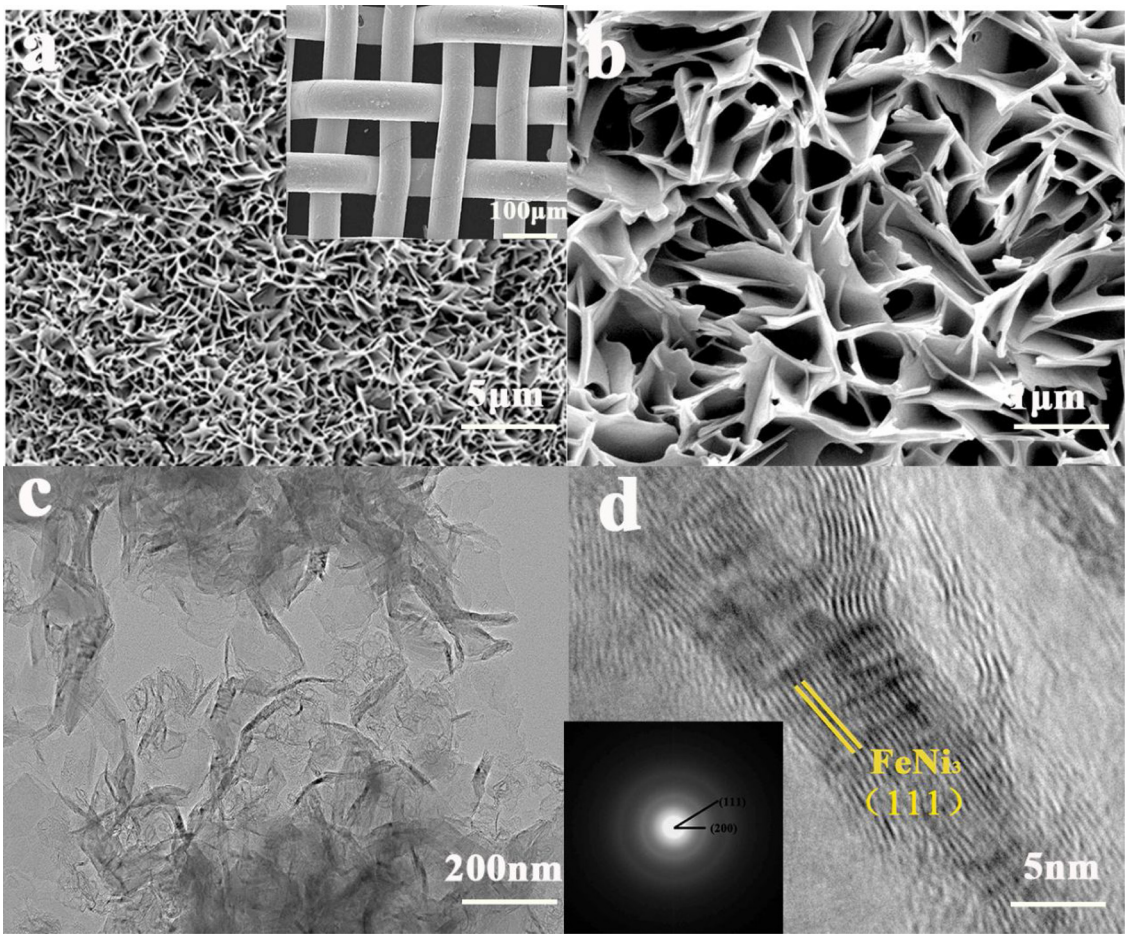

Fig. 2. The mesoporous $Ni_{0.8}Fe_{0.2}$ film: (a) FESEM image at lower magnification (see SLS in the inset); (b) FESEM image at higher magnification; (c) TEM image; (d) HRTEM showing lattice fringes (see SAED pattern in the inset).

transmission electron microscope (TEM) as shown in Fig. 2. From the inset in Fig. 2a, it can be observed that the mesoporous $Ni_{0.8}Fe_{0.2}$ film was successfully electrodeposited on SLS. As displayed in Fig. 2a and b at low and high magnifications, mesoporous $Ni_{0.8}Fe_{0.2}$ film was indeed composed of relatively uniformly distributed nanosheet-like structures. After etching surface of the as-prepared sample, the thickness of nanosheet is 150–200 nm. Fig. 2c depicts the TEM image of as-prepared mesoporous $Ni_{0.8}Fe_{0.2}$ film exfoliated by ultrasonic waves. From the TEM image at high magnification in the Fig. S3, the relatively bright (pores) and black regions of as-prepared sample can be clearly seen, suggesting the mesoporous structure [39]. HRTEM image with higher magnification (Fig. 2d) indicates that the $Ni_{0.8}Fe_{0.2}$ nanosheets show lattice fringes with a d-spacing of 0.204 nm, which are assigned to (111) crystal faces of $FeNi_3$ (JCPDS No. 38–0419). Selective area electron diffraction (SAED) pattern of the sample in the inset of Fig. 2d could be indexed into (111) and (200), which is consistent with XRD pattern (see Fig. 3a). To further investigate the elemental distribution, EDX elemental mapping (Fig. S5) was used for determining the approximate stoichiometry of Ni and Fe. The results demonstrated that Fe and Ni elements were distributed in the ratio of about 1: 4.

The crystalline phases were determined by X-ray diffraction (XRD) as shown in Fig. 3a. The results show that the diffraction peak located at 44.2° can be assigned to (111) lattice planes of $FeNi_3$ (PDF card: 38-0419) and (011) lattice planes of Ni (PDF card:04-0850). Besides, the peak at 51.6° is well defined and can be assigned to the (200) lattice plane of $FeNi_3$ and confirming the phase purity of the as-prepared films

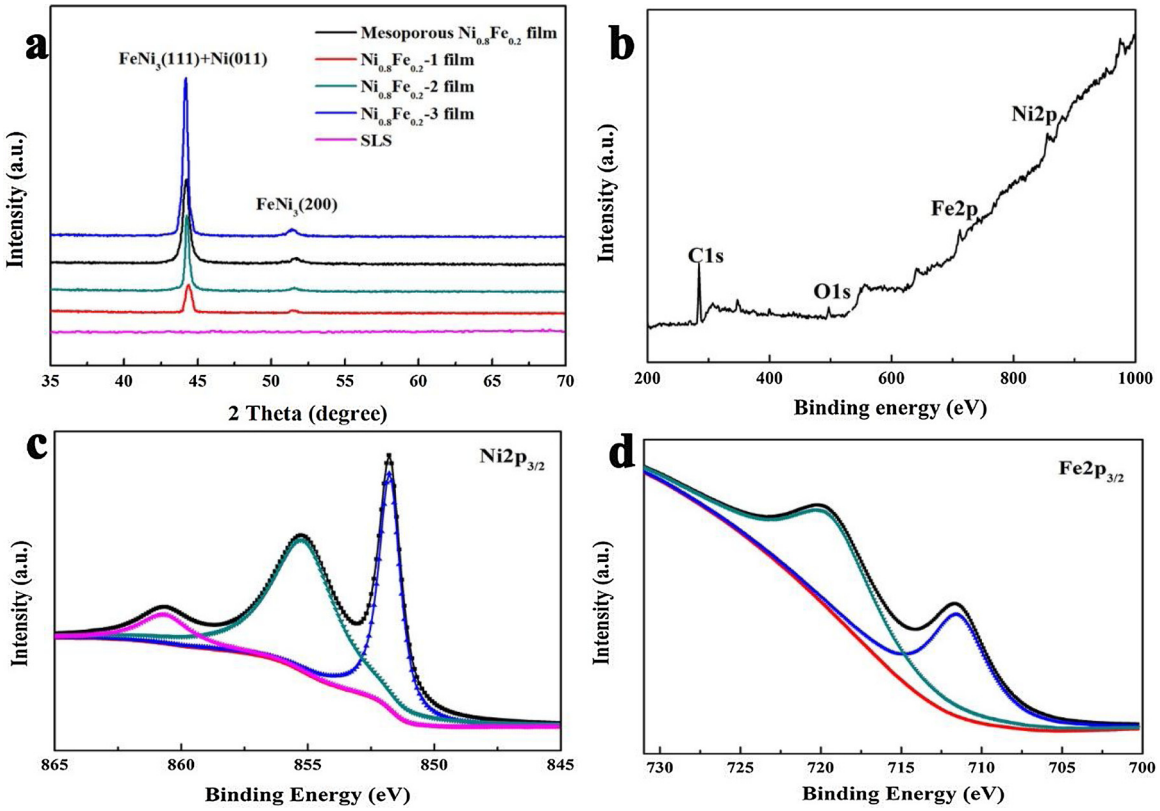

Fig. 3. XRD and XPS characterization of mesoporous $Ni_{0.8}Fe_{0.2}$ film (a) XRD patterns; (b) XPS survey spectrum; (c) Ni 2p spectrum; (d) Fe 2p spectrum.

Table 1
Comparison of Ni and Fe atomic composition determined by XPS and EDS.

	EDS		XPS	
	Ni	Fe	Ni	Fe
NiFe-2 film	79.39%	20.61%	78.71%	21.29%
Mesoporous NiFe film	79.92%	20.08%	78.63%	21.37%

on SLS. The particle size of mesoporous $Ni_{0.8}Fe_{0.2}$ film on SLS was calculated to be 8.1 nm from XRD peaks. All the XRD patterns of other as-prepared samples are also shown in Fig. 3a. It can be observed that all the synthetic materials showed crystalline $FeNi_3$. The survey X-ray photoelectron spectrum (XPS) of mesoporous $Ni_{0.8}Fe_{0.2}$ film is displayed in Fig. 3b, where a series of peaks related to O, C, Fe and Ni elements can be seen. Fig. 3c shows the high-resolution peak of Ni $2p_{3/2}$ with two principal peaks occurring at 852.4 and 855.6 eV, which can be attributed to metallic state Ni and Ni oxides/hydroxides, respectively, while a satellite peak of Ni $2p_{3/2}$ occurs at 862.6 eV. From Fig. 3d, the binding energies of Fe $2p_{3/2}$ can be seen at about 706.5 and 711.1 eV, which can be assigned to metallic state Fe and Fe oxides/hydroxides, respectively. As has been reported previously the surface of NiFe film exists as oxide because of Ni and Fe oxidation when exposed to air [40,41]. In addition, the composition of Ni and Fe atoms measured by XPS and EDS (Figs. S6 and S7) is shown in Table 1. We conclude that the ratio of nickel and iron is about 0.8:0.2, which did not change significantly after the removal of template.

N_2 adsorption/desorption was used to determine the mesoporous nature of films. Fig. 3e and f show the adsorption/desorption isotherms and the pore sizes of SLS substrate as control, $Ni_{0.8}Fe_{0.2}$-2 film and mesoporous $Ni_{0.8}Fe_{0.2}$ film, respectively. We found that the specific surface area of mesoporous $Ni_{0.8}Fe_{0.2}$ film reached 106.3 $m^2 g^{-1}$, which is approximately 7 times that of SLS substrate and 3 times that of $Ni_{0.8}Fe_{0.2}$-2 film. The adsorption-desorption isotherms of mesoporous $Ni_{0.8}Fe_{0.2}$ film belongs to type-IV with hysteresis, suggesting a typical feature of mesoporous material [42]. The mesoporous structure was evidently caused by the removal of Zn template and highly porous nature of nanosheets. The large specific surface area and appropriate pore size not only lead to fast release of O_2 during oxygen evolution reaction, but they also facilitate diffusion of electrons and OH^-. Besides, large specific surface area can also provide a great deal of active sites and more defects resulting in excellent OER activities [43]. The detailed adsorption-desorption and pore-size information of the three samples is shown in Figs. 3e and f and S8-10.

We have analyzed the OER performance of the mesoporous $Ni_{0.8}Fe_{0.2}$ binder-free electrode in O_2-saturated 1.0 M KOH solution under standard three-electrode system. Fig. 4 reveals the electrocatalytic OER performance of as-obtained samples. The iR-corrected polarization curves tested at a scan rate of 5 mV s^{-1} are displayed in Fig. 4a. As has been reported previously by others, the OER catalytic activity was estimated via the potential at the current density of 10 mA cm^{-2} [44]. It can be clearly observed (Fig. 4b) that mesoporous $Ni_{0.8}Fe_{0.2}$ electrode showed a low overpotential of 1.436 V (vs. RHE) at 10 mA cm^{-2}, whereas the $Ni_{0.8}Fe_{0.2}$ -1/2/3 films and SLS led to potentials of 1.555 V, 1.5018 V, 1.594 V and 1.567 V, respectively. The state-of-the-art IrO_2/C material exhibits a potential of 1.541 V at the current density of 10 mA cm^{-2}, which is much higher than that of mesoporous $Ni_{0.8}Fe_{0.2}$ electrode. Besides, we also test the LSV of mesoporous $Ni_{0.8}Fe_{0.2}$ -1 film and mesoporous $Ni_{0.8}Fe_{0.2}$ -3 film, which are shown in the Fig. S11. The OER properties were not better than that of mesoporous $Ni_{0.8}Fe_{0.2}$ -3 film. Moreover, Tafel plots were investigated and are shown in Fig. 4b to further characterize the OER performance. We fit the linear portions of polarization curves through Tafel equation: $\eta = b \log j + a$ where η is the overpotential, j is the current density, and b is the Tafel slope [45]. The as-obtained mesoporous $Ni_{0.8}Fe_{0.2}$ electrode showed the lowest Tafel slope of 64 mV dec^{-1} among all the samples. It can be clearly seen from Fig. 4c, that the use of template markedly decreased the Tafel slopes from 89 mV dec^{-1} ($Ni_{0.8}Fe_{0.2}$-2

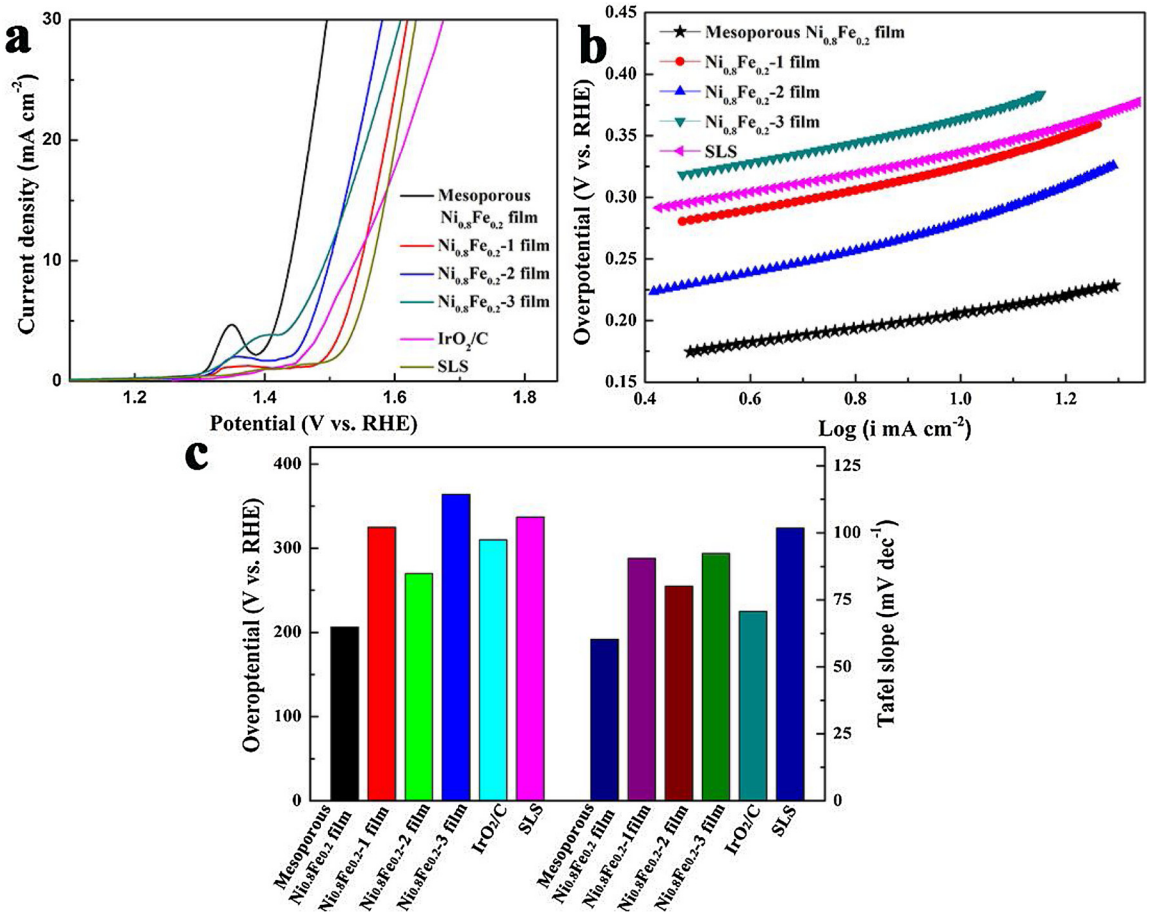

Fig. 4. OER activity of mesoporous $Ni_{0.8}Fe_{0.2}$ film, $Ni_{0.8}Fe_{0.2}$ film-1, film-2 and film-3, SLS and IrO_2/C measured in 1.0 M KOH: (a) their iR corrected polarization curves; (b) their Tafel plots; (c) comparison of their OER activity.

film) to 64 mV dec^{-1} (mesoporous $Ni_{0.8}Fe_{0.2}$ film). The above results clearly show that the mesoporous $Ni_{0.8}Fe_{0.2}$ electrode possessed high electrocatalytic activity and relatively low OER kinetics in contrast to other samples. We suggest that the significantly improved OER activity can be attributed to (1) novel synthetic process and (2) porous structure as discussed below: (1) During hydrothermally driven electrodeposition method, the higher temperature makes the H_2 generated on the cathode overflow faster. Also, higher hydrothermal temperature facilitates water to volatilize and generate high pressure environment. The scouring of gas and pressure facilitate the formation of more active sites on the coating surfaces. From the SEM image (Fig. S14), we can see that NiFe film electrodeposited by traditional method shows fewer active sites leading to poor catalytic performance compared with the mesoporous $Ni_{0.8}Fe_{0.2}$ electrode; (2) Porous structure not only can expose high surface of the catalyst for reaction, but it also leads to faster diffusion of electrolyte through pores and therefore, the porous materials have excellent reactivity. The above two properties explain why $Ni_{0.8}Fe_{0.2}$-2 electrode showed excellent OER activities compared with $Ni_{0.8}Fe_{0.2}$-1, 3 electrodes and SLS. The coating of $Ni_{0.8}Fe_{0.2}$-1 electrode was too thin to provide active sites. Therefore, the catalytic activity was only slightly higher than that of SLS. On the contrary, $Ni_{0.8}Fe_{0.2}$-3 electrode, which had relatively thick coating after 30 min of electrodeposition also did not show high OER activity because apparently the surface layers only could react with electrolyte. As a result, the oxygen evolution reaction was not good in this case. Mesoporous $Ni_{0.8}Fe_{0.2}$ electrode developed here also showed enhanced OER performance in alkaline electrolyte when compared to other NiFe-based electrocatalysts reported in the recent literature as given in Table 2.

The electrochemical active surface area (ECSA) measurement could be used to estimate catalytic activity and here, it was determined by the double layer capacitance (C_{dl}), which is calculated from the slope of the plot of scan rate as a function of current density [60,61]. To further verify the effects of porous structure on OER properties, the ECSA

Table 2
Comparison of overpotential of this work with those from others for NiFe-based OER electrocatalysts in alkaline solution.

Catalysis	Electrolyte	Overpotential (η_{given}/mv)	Refs.
Mesoporous $Ni_{0.8}Fe_{0.2}$ film	**1 M KOH**	**η_{10} = 206**	**This work**
NiFe alloy/C	1 M KOH	η_{20} = 224	[27]
NiFe nanorod	1 M KOH	η_{10} = 347	[33]
NiFe-LDH HMS	1 M KOH	η_{10} = 239	[34]
NiFe MMO/CNT	1 M KOH	η_{10} = 260	[46]
NiFe alloy	1 M KOH	η_{10} = 370	[47]
NiFe-DAT	1 M NaOH	η_{100} = 300	[48]
Ni–FeOx@GO	0.1 M KOH	η_{10} = 337	[49]
NiFe NPS	1 M KOH	η_{10} = 237	[50]
NiFe NO_3	0.1 M KOH	η_{10} = 290	[51]
NiFe-LDH/NrGO	1 M KOH	η_{10} = 250	[52]
Mesoporous $Ni_{60}Fe_{30}Mn_{10}$-alloy	1 M KOH	η_{10} = 350	[53]
Ni-Fe disulfide@ oxyhydroxide	1 M KOH	η_{10} = 230	[57]
$FeNiS_2$ nanosheet	1 M KOH	η_{10} = 310	[58]
N-NiFe LDH	1 M KOH	H_{10} = 210	[59]
NiFe LDH/CNT	1 M KOH	η_{10} = 230	[60]
$NaNi_{0.9}Fe_{0.1}O_2$	1 M KOH	η_{10} = 290	[61]
NiFe nanoparticles	1 M KOH	η_{10} = 330	[62]

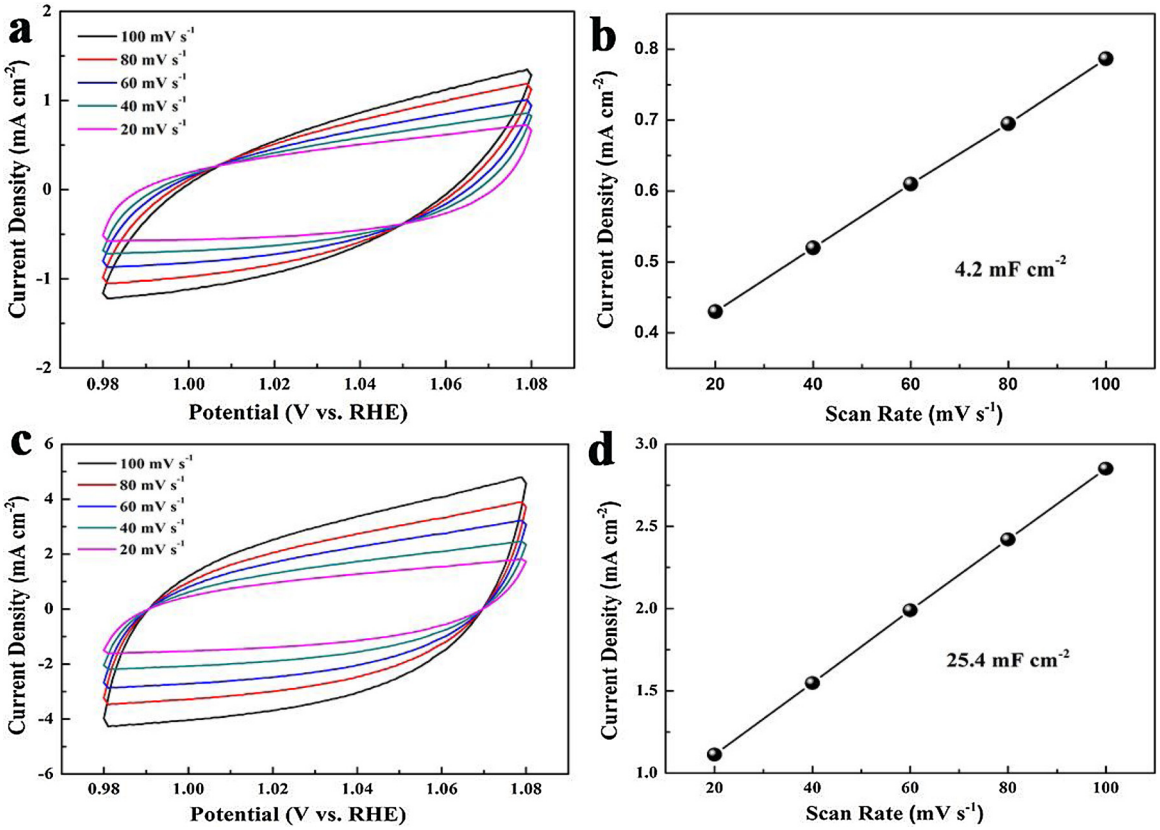

Fig. 5. Cyclic voltammetry curves of (a) $Ni_{0.8}Fe_{0.2}$-2 film electrode and (c) mesoporous $Ni_{0.8}Fe_{0.2}$ film electrode, which are analyzed at various scan rates from 20 to 100 mV s^{-1}. Also shown is the scan rate dependence of the current densities of (b) $Ni_{0.8}Fe_{0.2}$-2 film electrode and (d) mesoporous $Ni_{0.8}Fe_{0.2}$ film electrode.

characterization of different materials is shown in Fig. 5. Fig. 5a and c display the CV curves of $Ni_{0.8}Fe_{0.2}$-2 film electrode and mesoporous $Ni_{0.8}Fe_{0.2}$ film electrode at various scan rates from 20 to 100 mV s^{-1}, respectively. It can be clearly seen that the C_{dl} of mesoporous $Ni_{0.8}Fe_{0.2}$ film electrode is 25.3 mF cm^{-2}, which is 6 times that of $Ni_{0.8}Fe_{0.2}$ traditional film electrode (4.2 mF cm^{-2}). As observed before [54–56], we may conclude that the higher Cdl value of mesoporous $Ni_{0.8}Fe_{0.2}$ is due to its porous structure. The above comparisons reveal that mesoporous $Ni_{0.8}Fe_{0.2}$ film electrode possesses larger electrochemical active area, suggesting more effective accessibility of active sites and better catalytic performance. These results demonstrate that porous structure can enhance the OER properties, which also match with the results of polarization curve and Tafel plot.

Stability test of electrocatalyst is an important factor for OER properties. Long term durability of mesoporous $Ni_{0.8}Fe_{0.2}$ electrode and traditional electrodeposited $Ni_{0.8}Fe_{0.2}$ electrode are examined by chronopotentiometry at a constant anodic current density of 10 mA cm^{-2} for a period of 2×10^5 s (more than 55 h). The mesoporous $Ni_{0.8}Fe_{0.2}$ electrode exhibited (Fig. 6a) a good stability with a minor change from 1.436 V to 1.445 V (only 0.8% loss after long term OER operation). The polarization curve after OER test (Fig. S13) showed little or no difference from the initial curve. The above result is superior to the recently reported results of NiFe based OER electrocatalysts [57–68]. On the contrary, traditional electrodeposited $Ni_{0.8}Fe_{0.2}$ electrode shows a poor durability with potential change from 1.584 V to 1.688 V (Fig. 6a) and the catalytic activity apparently decreases after 1.5×10^5 s. Excellent catalytic performance of mesoporous $Ni_{0.8}Fe_{0.2}$ electrode may be attributed to its porous structure and good crystallinity. It is a common knowledge that oxygen gas bubbles generated during chronopotentiometry test make active materials peel off from the surface of electrode. Additionally, oxygen bubbles increasingly accumulate and hinder the electrolyte contact with catalyst, causing an increase of overpotential [35,36]. Porous structure can expedite the detachment of bubbles from the electrode surface and their diffusion into the electrolyte. In addition, porous structure is beneficial for gas release and also prevents loss of active materials. Besides, electrodeposition of Ni-Fe film directly on stainless steel wire without binders can efficiently improve the stability of the film [65]. The XRD patterns of two samples are shown in Fig. 6b. The particle size of mesoporous $Ni_{0.8}Fe_{0.2}$ film (8.1 nm) is larger than that of traditionally electrodeposited $Ni_{0.8}Fe_{0.2}$ film (2.3 nm). Based on the above XRD results, we conclude that crystallization of $Ni_{0.8}Fe_{0.2}$ film electrodeposited under hydrothermal condition improved significantly. The chronopotentiometry study of mesoporous $Ni_{0.8}Fe_{0.2}$ electrode at different anodic current densities (j = 10, 20, 30, 40 and 50 mA cm^{-2}) is displayed in Fig. 6c, revealing a relatively stable potentiometric response. We also designed alkaline water splitting cell (Fig. 6d) using the mesoporous $Ni_{0.8}Fe_{0.2}$ film supported on SLS as anode and Pt plate as cathode. It can be clearly observed (Fig. 6d) that abundant gas bubbles were generated from mesoporous $Ni_{0.8}Fe_{0.2}$ electrode, indicating good OER activity.

To further examine the sluggish charge transfer of as-prepared samples, electrochemical impedance spectroscopy (EIS) test was conducted in Fig. 7. All the samples exhibited similar semicircles located in high frequency region (Fig. 7). The equivalent circuit fitted by the EIS patterns is displayed in Fig. S15. R_s and R_{ct} represent the bulk solution resistance and the charge transfer resistance, respectively. It can be seen that the solution resistance of all samples is about 1.95 Ω. The Nyquist plots showed that the R_{ct} values of mesoporous $Ni_{0.8}Fe_{0.2}$ film electrode, $Ni_{0.8}Fe_{0.2}$-1/2/3 film electrodes and SLS are as low as 2.76 Ω, 3.23 Ω, 2.91 Ω, 3.13 Ω and 3.63 Ω, respectively. The mesoporous $Ni_{0.8}Fe_{0.2}$ electrode delivers the lowest R_{ct}, indicating the quickest charge transfer capability and facilitated the highest OER activity among all five electrocatalysts [66]. The low charge transfer resistance can be attributed

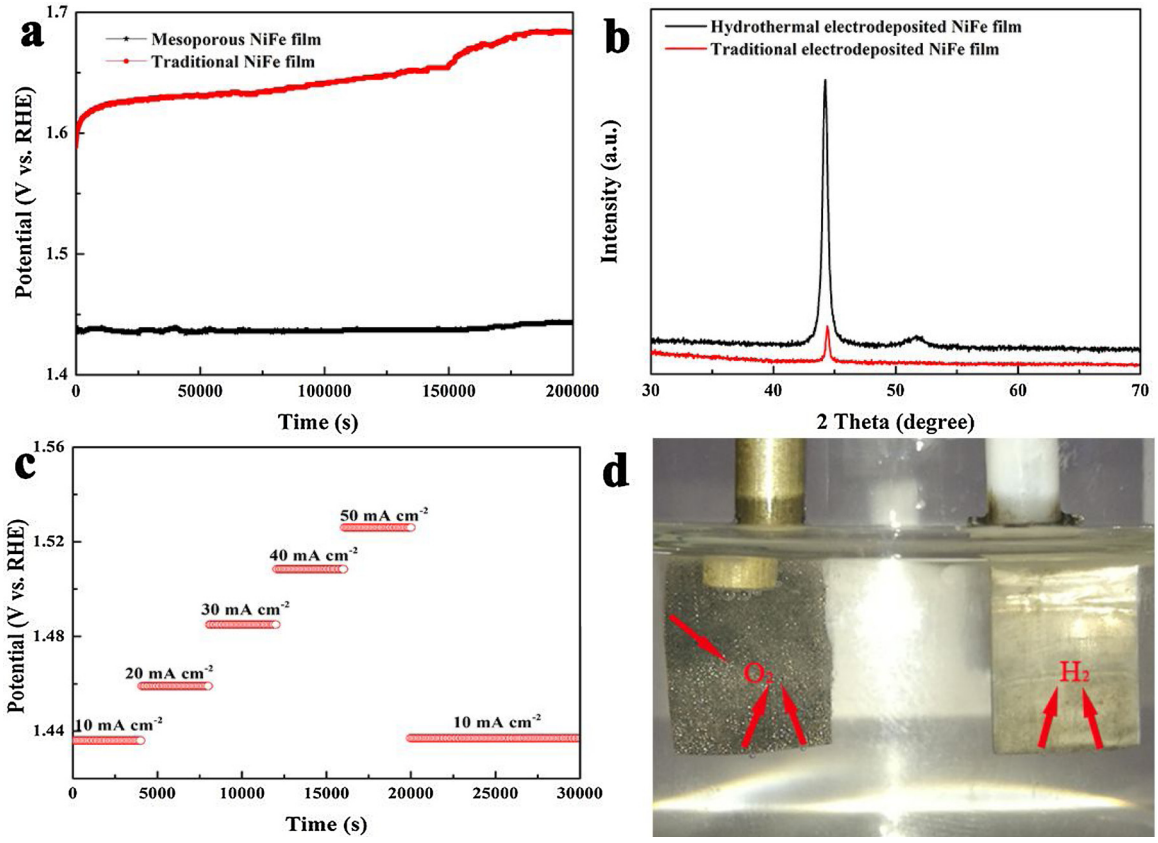

Fig. 6. (a) Chronopotentiometry test of mesoporous $Ni_{0.8}Fe_{0.2}$ electrode and electrode prepared at industrial condition at 10 mA cm^{-2} in 1 M KOH solution.(b) Chronopotentiometry test of mesoporous $Ni_{0.8}Fe_{0.2}$ electrode at j = 10, 20, 30, 40 and 50 100 mA cm^{-2}; (c) Multi-step chronopotentiometric test in 1.0 M KOH at different current densities (d) water-splitting system.

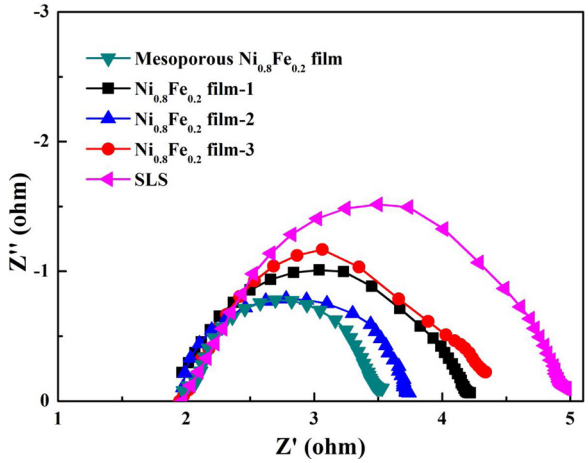

Fig. 7. Electrochemical impedance spectra of mesoporous $Ni_{0.8}Fe_{0.2}$ film, $Ni_{0.8}Fe_{0.2}$-1/2/3 film and SLS.

to the porous structure with abundant active sites and conductive substrate. The porous structure also facilitates OER catalyst contact with electrolyte and creates expedited charge transport pathways. The low resistance can provide a faster OER kinetics and significantly improve the OER property [67,68].

4. Conclusion

In summary, we developed a novel hydrothermal elctrodeposition method for the first time to prepare mesoporous $Ni_{0.8}Fe_{0.2}$ film self-supported electrode as oxygen evolution reaction catalyst. Mesoporous $Ni_{0.8}Fe_{0.2}$ film showed significantly enhanced electrochemical active area of 25.3 mF cm^{-2}, a low overpotential 206 mV at 10 mA cm^{-2} and a small Tafel slope of 64 mV dec^{-1}. It showed a good retention rate of OER activity after 2×10^5 s (more than 55 h) at 10 mA cm^{-2}. Hydrothermal electrodeposition method has been demonstrated to significantly enhance abundant active sites and improve crystallization of $Ni_{0.8}Fe_{0.2}$ film. Besides, porous structure provided highly exposed active sites and fast gas release and mass transport, which are beneficial for OER performance. The low cost and high catalytic activity of mesoporous $Ni_{0.8}Fe_{0.2}$ film as binder-free electrode developed here provides a new strategy to fabricate mesoporous alloy films for OER in water splitting systems.

Appendix A. Supplementary data

Supplementary material related to this article can be found, in the online version, at doi:https://doi.org/10.1016/j.apcatb.2018.04.009.

References

[1] M. Dresselhaus, I. Thomas, Nature 414 (2001) 332–337.
[2] H. Wang, H. Dai, Chem. Soc. Rev. 42 (2013) 3088–3113.
[3] N. Wang, M. Yao, P. Zhao, W. Hu, S. Komarneni, J. Mater. Chem. A 5 (2017) 5838–5845.
[4] A. Pendashteh, J. Palma, M. Andersona, R. Marcill, Appl. Cata. B- Environ. 201 (2017) 241–252.
[5] Y. Gu, S. Chen, J. Ren, Y.A. Jia, C. Chen, S. Komarneni, D. Yang, X. Yao, ACS Nano 12 (2018) 245–253.
[6] Q. Lu, Y. Yu, Q. Ma, B. Chen, H. Zhang, Adv. Mater. 28 (2016) 1917–1933.
[7] B. Zhang, J. Liu, S. Yue, Y. Teng, Z. Wang, X. Li, S. Qu, Z. Wang, Appl. Cata. B-Environ. 219 (2017) 432–438.
[8] D.G.H. Hetterscheid, J.N.H. Reek, Angew. Chem. Int. Ed. 51 (2012) 9740–9747.
[9] R. Cao, W.Z. Lai, P. Du, Energy Environ. Sci. 5 (2012) 8134–8157.
[10] Y. Cheng, C. Xu, L. Jia, J.D. Gale, L. Zhang, C. Liu, P. Shen, S. Jiang, Appl. Cata. B-

Environ. 163 (2015) 96–104.
[11] S. Park, Y. Shao, J. Liu, Y. Wang, Energy Environ. Sci. 5 (2012) 9331–9344.
[12] S. Siracusano, N.V. Dijk, E. Payne-Johnson, V. Baglio, A.S. Aricò, Appl. Cata. B-Environ. 164 (2015) 488–495.
[13] Y. Lee, J. Suntivich, K.J. May, E.E. Perry, Y. Shao-Horn, J. Phys. Chem. Lett. 3 (2012) 399–404.
[14] J. Zhang, Z. Zhao, Z. Xia, L. Dai, Nat. Nanotechnol. 10 (2015) 444.
[15] C.O. Ania, M. Seredych, E. Rodriguez-Castellon, T.J. Bandosz, Appl. Cata. B-Environ. 163 (2015) 424–435.
[16] M. Gong, Y. Li, H. Wang, Y. Liang, J. Wu, J. Zhou, J. Wang, T. Regier, F. Wei, H. Dai, J. Am. Chem. Soc. 135 (2013) 8452–8456.
[17] Y. Qiu, L. Xin, W. Li, Langmuir 30 (2014) 7893–7901.
[18] L. Han, S. Dong, E. Wang, Adv. Mater. 28 (2016) 9266–9291.
[19] H. Osgooda, S.V. Devaguptapua, H. Xub, J. Choc, G. Wu, Nano Today 11 (2016) 601–625.
[20] L. Dua, L. Luo, Z. Feng, M. Engelhard, X. Xie, B. Han, J. Sun, J. Zhang, G. Yin, C. Wang, Y. Wang, Nano Energy 39 (2017) 245–252.
[21] E. Nurlaela, T. Shinagawa, M. Qureshi, D.S. Dhawale, K. Takanabe, ACS Catal. 6 (2016) 1713–1722.
[22] X. Jia, Y. Zhao, G. Chen, L. Shang, R. Shi, X. Kang, G.I.N. Waterhouse, L. Wu, C. Tung, T. Zhang, Adv. Energy Mater. 6 (2016) 1502585.
[23] B. Li, S. Zhang, C. Tang, X. Cui, Q. Zhang, Small 13 (2017) 1700610.
[24] X. Xu, F. Song, X. Hu, Nat. Commun. 7 (2016) 12324–12330.
[25] Y. Hou, M.R. Lohe, J. Zhang, S. Liu, X. Zhuang, X. Feng, Energ. Environ. Sci. 9 (2016) 478–483.
[26] S. Chen, J. Duan, M. Jaroniec, S. Qiao, Angew. Chem., Int. Ed. 52 (2013) 13567–13570.
[27] Y. Feng, H. Zhang, L. Fang, Y. Mu, Y. Wang, ACS Catal. 6 (2016) 4477–4485.
[28] H. Zhang, W. Tian, L. Zhou, H. Sun, M. Tade, S. Wang, Appl. Cata. B- Environ. 223 (2018) 2–9.
[29] M. Sun, S. Huang, L. Chen, Y. Li, X. Yang, Z. Yuan, B. Su, Chem. Soc. Rev. 45 (2016) 3479–3563.
[30] M. Yao, N. Wang, W. Hu, J. Electroanal. Chem. 782 (2016) 133–137.
[31] N. Ma, Y. Jia, X. Yang, X. She, L. Zhang, Z. Peng, X. Yao, D. Yang, J. Mater. Chem. A 4 (2016) 6376–6384.
[32] H. Wang, F. Yin, B. Chen, X. He, P. Lv, C. Ye, D. Liu, Appl. Cata. B- Environ. 205 (2017) 55–67.
[33] G. Liu, K. Wang, X. Gao, D. He, J. Li, Electrochim. Acta 211 (2016) 871–878.
[34] C. Zhang, M. Shao, L. Zhou, Z. Li, K. Xiao, M. We, A.C.S. Appl. Mater. Inter. 8 (2016) 33697–33703.
[35] X. Lu, C. Zhao, Nat. Commun. 6 (2015) 6616.
[36] S.H. Ahna, I. Choia, H. Parka, S. Hwanga, S. Yooa, E. Choa, H. Kima, D. Henkensmeiera, S. Nama, S. Kim, J. Jang, Chem. Commmun. 49 (2013) 9323–9325.
[37] K. Li, D. Xue, J. Phys. Chem. A 110 (2006) 11332–11337.
[38] M. Ledendecker, G. Clavel, M. Antonietti, M. Shalom, Adv. Funct. Mater. 25 (2015) 393–399.
[39] N. Wang, P. Zhao, K. Liang, M. Yao, Y. Yang, W. Hu, Chem. Eng. J. 307 (2017) 105–112.
[40] S. Ci, Mao S, Hou Y, S. Cui, H. Kim, R. Ren, Z. Wen, J. Chen, J. Mater. Chem. A 3 (2015) 7986–7993.
[41] Y. Feng, X. Yu, U. Paik, Sci. Rep.-UK 6 (2016) 34004.
[42] N. Wang, P. Zhao, Q. Zhang, M. Yao, W. Hu, Compos. Part B-Eng. 113 (2017) 144–151.
[43] S. Cai, Z. Meng, H. Tang, Y. Wang, P. Tsiakaras, Appl. Cata. B- Environ. 217 (2017) 477–484.
[44] N. Suen, S. Hung, Q. Quan, N. Zhang, Yi. Xu, H. Chen, Chem. Soc. Rev. 46 (2017) 337–365.
[45] Y. Fan, S. Ida, A. Staykov, T. Akbay, H. Hagiwara, J. Matsuda, K. Kaneko, T. Ishihara, Small 13 (2017) 1700099.
[46] Y. Li, H. He, W. Fu, C. Mu, X. Tang, Z. Liu, D. Chi, X. Hu, Chem. Sci. 52 (2016) 1439–1442.
[47] C. Xie, Y. Wang, K. Hu, L. Tao, X. Huang, J. Huo, S. Wang, J. Mater. Chem. A 5 (2017) 87–91.
[48] T.T.H. Hoang, A.A. Gewirth, ACS Catal. 6 (2016) 1159–1164.
[49] C. Tang, H. Wang, H. Wang, Q. Zhang, G. Tian, J. Nie, F. Wei, Adv. Mater. 27 (2015) 4516–4522.
[50] S.L. Candelaria, N.M. Bedford, T.J. Woehl, N.S. Rentz, A.R. Showalter, S. Pylypenko, B.A. Bunker, S. Lee, B. Reinhart, Y. Ren, S.P. Ertem, E.B. Coughlin, N.A. Sather, J.L. Horan, A.M. Herring, L.F. Greenlee, ACS Catal. 7 (2017) 365–379.
[51] C. Andronescua, S. Barwea, E. Ventosaa, J. Masaa, E. Vasiled, B. Konkenaa, S. Möllera, W. Schuhmann, Angew. Chem. Int. Ed. 56 (2017) 11258–11262.
[52] T. Zhan, X. Liu, S. Lu, W. Hou, Appl. Cata. B- Environ. 205 (2017) 551–558.
[53] E. Detsi, J.B. Cook, B.K. Lesel, C.L. Turner, Y. Liang, S. Robbennolt, S.H. Tolbert, Energy Environ. Sci. 9 (2016) 540–549.
[54] K. Li, D. Xue, J. Mater. Chem. A 4 (2016) 7522–7537.
[55] K. Li, D. Xue, Mater. Res. Bull. 83 (2016) 201–206.
[56] K. Li, D. Xue, J. Materiomics 1 (2015) 170–187.
[57] M. Zhou, Q. Weng, X. Zhang, X. Wang, Y. Xue, X. Zeng, Y. Bando, D. Golberg, J. Mater. Chem. A 5 (2017) 4335–4342.
[58] J. Jiang, S. Lu, H. Gao, X. Zhang, H. Yu, Nano Energy 27 (2016) 526–534.
[59] S. Chen, J. Duan, P. Bian, Y. Tang, R. Zheng, S. Qiao, Adv. Energy Mater. 5 (2015) 1500936.
[60] M. Gong, Y. Li, H. Wang, Y. Liang, J.Z. Wu, J. Zhou, J. Wang, T. Regier, F. Wei, H. Dai, J. Am. Chem. Soc. 135 (2013) 8452–8455.
[61] B. Weng, F. Xu, C. Wang, W. Meng, C.R. Grice, Y. Yan, Energy Environ. Sci. 10 (2017) 121–128.
[62] X. Zhang, H. Xu, X. Li, Y. Li, T. Yang, Y. Liang, ACS Catal. 6 (2016) 580–588.
[63] S. Bae, J. Kim, H. Randriamahazaka, S. Moon, J. Park, I. Oh, Adv. Energy Mater. 7 (2017) 1601492.
[64] P. He, X. Yu, X. Lou, Angew. Chem. Int. Ed. 129 (2017) 3955.
[65] N. Wang, B. Sun, M. Yao, W. Hu, S. Komarneni, Chem. Eng. J. (2018), http://dx.doi.org/10.1016/j.cej.2018.03.147.
[66] M. Yao, N. Wang, W. Hu, J. Mater. Sci-Mater. El. 28 (2017) 11119–111124.
[67] M. Balogun, W. Qiu, H. Yang, W. Fan, Y. Huang, P. Fang, G. Li, H. Ji, Y. Tong, Energy Environ. Sci. 9 (2016) 3411–3416.
[68] S. Jing, L. Zhang, L. Luo, J. Lu, S. Yin, P. Shen, P. Tsiakaras, Appl. Cata. B- Environ. 224 (2018) 533–540.

Update

Applied Catalysis B: Environmental

Volume 243, Issue , April 2019, Page 802–803

DOI: https://doi.org/10.1016/j.apcatb.2018.06.038

Applied Catalysis B: Environmental 243 (2019) 802–803

Contents lists available at ScienceDirect

Applied Catalysis B: Environmental

journal homepage: www.elsevier.com/locate/apcatb

Corrigendum

Corrigendum to "Novel hydrothermal electrodeposition to fabricate mesoporous film of $Ni_{0.8}Fe_{0.2}$ nanosheets for high performance oxygen evolution reaction" [Appl. Catal. B: Environ. 233 (2018) 226–233]

Mengqi Yao[a], Ni Wang[a,b], Wencheng Hu[a,*], Sridhar Komarneni[b,*]

[a] Center for Applied Chemistry, University of Electronic Science & Technology of China, Chengdu, China
[b] Materials Research Institute and Department of Ecosystem Science and Management, Materials Research Laboratory, The Pennsylvania State University, PA, USA

Regrettably, the authors need to make the following corrections for the above published article:

1. The authors' affiliation "Center of Applied Chemistry, University of Electronic Science & Technology of China, Chengdu, China" should be corrected to "Center for Applied Chemistry, University of Electronic Science & Technology of China, Chengdu, China.".

2. Fig. 3 was incomplete in the original article. Correct version of Fig. 3 is given below:

DOI of original article: https://doi.org/10.1016/j.apcatb.2018.04.009
* Corresponding authors.
E-mail addresses: huwc@uestc.edu.cn (W. Hu), sxk7@psu.edu (S. Komarneni).

https://doi.org/10.1016/j.apcatb.2018.06.038

Available online 29 August 2018

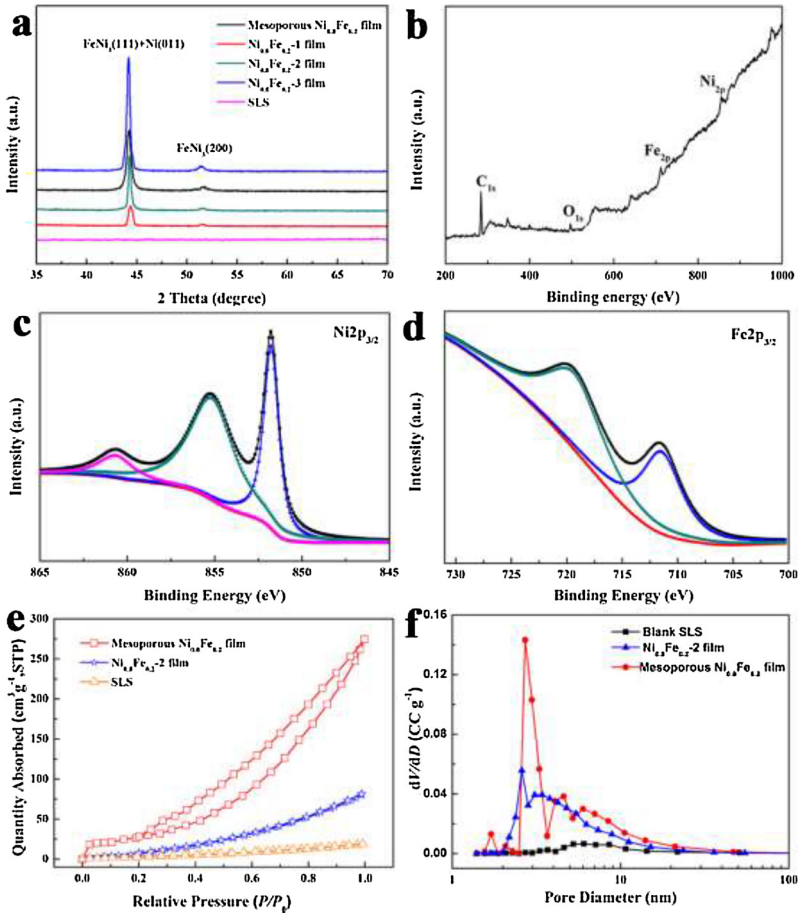

Fig. 3 XRD and XPS characterization of mesoporous $Ni_{0.8}Fe_{0.2}$ film (a) XRD pattern; (b) XPS survey spectrum; (c) Ni 2p spectrum; (d) Fe 2p spectrum; (e) N_2 adsorption–desorption isotherms of mesoporous $Ni_{0.8}Fe_{0.2}$ film, $Ni_{0.8}Fe_{0.2}$-2 film and SLS; (f) the corresponding pore size distribution as determined by BJH of the above samples.

3. On p. 230 the cited references [60,61] should be corrected to [63,64].

4. On p. 231 the cited references [57–68] should be corrected to [57–59].

Authors would like to apologize for the inconvenience caused.